arXiv:1610.07139v1 [astro-ph.SR] 23 Oct 2016

A Monte Carlo Study of Flux Ratios of Raman Scattered O VI Features at 6825 Å and 7082 Å in Symbiotic Stars

Young-Min Lee, Dae-Sub Lee, Seok-Jun Chang, Jeong-Eun Heo, Hee-Won Lee
Department of Physics and Astronomy, Sejong University, Seoul, 05006, Korea

Narae Hwang, Byeong-Gon Park[1], Ho-Gyu Lee
Korea Astronomy and Space Science Institute, Daejon, 34055, Korea

ABSTRACT

Symbiotic stars are regarded as wide binary systems consisting of a hot white dwarf and a mass losing giant. They exhibit unique spectral features at 6825 Å and 7082 Å, which are formed via Raman scattering of O VI$\lambda\lambda$ 1032 and 1038 with atomic hydrogen. We adopt a Monte Carlo technique to generate the same number of O VIλ1032 and λ1038 line photons and compute the flux ratio $F(6825)/F(7082)$ of these Raman scattered O VI features formed in neutral regions with a simple geometric shape as a function of H I column density N_{HI}. In cylindrical and spherical neutral regions with the O VI source embedded inside, the flux ratio $F(6825)/F(7082)$ shows an overall decrease from 3 to 1 as N_{HI} increases in the range 10^{22-24} cm^{-2}. In the cases of a slab geometry and other geometries with the O VI source outside the H I region, Rayleigh escape operates to lower the flux ratio considerably. For moderate values of $N_{HI} \sim 10^{23}$ cm^{-2} the flux ratio behaves in a complicated way to exhibit a broad bump with a peak value of 3.5 in the case of a sphere geometry. We find that the ratio of Raman conversion efficiencies of O VI$\lambda\lambda$1032, 1038 ranges from 0.8 to 3.5. Our high resolution spectra of 'D' type HM Sge and 'S' type AG Dra obtained with the *Canada-France-Hawaii-Telescope* show that the flux ratio $F(6825)/F(7082)$ of AG Dra is significantly smaller than that of HM Sge, implying that 'S' type symbiotics are characterized by higher N_{HI} than 'D' type symbiotics.

Subject headings: radiative transfer – scattering – binaries: symbiotic stars

1. Introduction

Binary systems involving an accreting white dwarf are classified into cataclysmic variables and symbiotic stars, which constitute important candidates for Type Ia supernovae (e.g. Mikołajewska 2012). In cataclysmic variables, the secondary red dwarf star filling the Roche lobe injects its material through the inner Lagrangian point leading to formation of an accretion disk around the white dwarf primary (e.g. Warner 1995). In contrast, symbiotic stars consist of a compact star, mostly a white dwarf, and a giant star losing a large amount of mass in the form of a slow stellar wind. Some fraction of the slow stellar wind from the giant companion is gravitationally captured by the white dwarf (e.g. Mikołajewska 2012).

Activities associated with symbiotic stars include X-ray emission, erratic variabilities, prominent emission lines and collimated outflows (e.g. Angeloni et al. 2012; Zamanov et al. 2015). In particular, Angeloni et al. (2011) discovered a huge jet in Sanduleak's star. It is highly controversial whether an accretion disk is formed in a stable fashion in symbiotic stars. Hydrodynamical studies show the plausibility of an accretion disk and also some symbiotic stars are known to exhibit optical flickering indicating the presence of an accre-

[1]Korea University of Science and Technology (UST), Daejon, 34113, Korea

tion disk (e.g. Sokoloski et al. 2001; Sokoloski & Bildsten 2010).

Symbiotic stars are classified into 'S' type and 'D' type based on the spectral energy distribution in the IR region, where 'D' type symbiotics show an IR excess indicative of a dust component with a temperature $\sim 10^3$ K (e.g. Whitelock 1987; Angeloni et al. 2010). No such IR excess is apparent in 'S' type symbiotics. The orbital periods of 'D' type symbiotics are poorly known and are presumed to exceed several decades, implying that the giant companion is separated from the white dwarf by tens of AU. This is in high contrast in that many 'S' type symbiotics are known to have orbital periods of several hundreds of days, which points out that the giant companion is much closer to the white dwarf than their 'D' type counterparts.

A significant fraction of symbiotic stars exhibit unique broad emission features at 6825 Å and 7082 Å with a width $\sim 20 - 30$ Å. These mysterious spectral features were identified by Schmid (1989), who proposed that they are formed through Raman scattering of O VI$\lambda\lambda$ 1032 and 1038 with atomic hydrogen. Raman scattering proceeds with an incident far UV photon blueward of Lyα on a hydrogen atom in the ground state, which finally de-excites into the $2s$ state. As opposed to Raman scattering, the elastic version is Rayleigh scattering.

For an incident O VI line photon, the energy difference of the $1s$ and $2s$ states of a hydrogen atom is responsible for the creation of a Raman photon redward of Hα. More explicitly, an incident far UV photon with frequency ν_i can be Raman scattered to re-appear with frequency ν_0 given by

$$\nu_0 = \nu_i - \nu_{Ly\alpha} \tag{1}$$

where $\nu_{Ly\alpha}$ is the frequency of Lyα. To a frequency range around ν_i denoted by $\Delta\nu_i$ corresponds a frequency range $\Delta\nu_o$ around ν_o, where $\Delta\nu_o = \Delta\nu_i$. Therefore, we have

$$\frac{\Delta\nu_i}{\nu_i} = \left(\frac{\nu_o}{\nu_i}\right)\frac{\Delta\nu_o}{\nu_o}, \tag{2}$$

which explains the broad line widths exhibited by Raman scattered features (Nussbaumer et al. 1989).

The scattering cross section and the branching ratio of Raman scattering by atomic hydrogen are discussed in a number of research works including Schmid (1989), Nussbaumer et al. (1989) and Saslow & Mills (1969). Adopting the values of 1031.928Å and 1037.618 Å as center wavelengths of O VI resonance doublet (Moore 1979), the cross sections for Rayleigh and Raman scattering are

$$\sigma_{Ray}(1032) = 34.0\ \sigma_T,\ \sigma_{Ram}(1032) = 7.5\ \sigma_T$$
$$\sigma_{Ray}(1038) = 6.6\ \sigma_T,\ \sigma_{Ram}(1038) = 2.5\ \sigma_T \tag{3}$$

at line centers of O VI (Lee & Lee 1997a). Here, $\sigma_T = 0.665\times10^{-24}$ cm^2 is the Thomson scattering cross section.

Harries & Howarth (1996) presented their spectropolarimetric survey of Raman O VI 6825 and 7082 features in a large number of symbiotic stars. In their study, most Raman O VI fluxes show strong linear polarization with a degree of polarization amounting to $\sim$ 10 percent. In addition, the line profiles of these Raman features are characterized by double or triple peak structures. Another notable point is that the Raman O VI 6825 and 7082 features exhibit disparate profiles. In particular, usually the blue part of Raman 7082 feature is relatively more suppressed than its Raman 6825 counterpart. The profile disparity for Raman O VI features was also noted by other researchers including Schmid (1999), who proposed that the kinematics associated with the giant wind is mainly responsible for the multiple peak structures. Lee & Park (1999) advanced a view that the O VI emission region forms a part of the accretion flow around the white dwarf resulting in multiple peak profiles in Raman O VI features (see also Heo & Lee 2015).

Allen (1980) used spectrophotometric data of a few symbiotic stars to report that the Raman O VI feature at 6825 Å is about 4 times stronger than the 7082 feature on average. Schmid et al. (1999) presented their spectroscopic observations of several symbiotic stars to show that the flux ratio of Raman O VI at 6825 Å and 7082 Å ranges from around 2 to 7. In particular, 'D' type symbiotics such as RR Telescopii and V1016 Cygni exhibit high flux ratios whereas 'S' type symbiotics show low flux ratios. They attributed to this tendency to higher Raman conversion efficiency in 'S' type symbiotics than in 'D' type ones, where the Raman conversion efficiency is defined as the number ratio N(Ram)/N(O VI) between the Raman scattered photons and the incident O VI line photons.

Considering the role played by the Raman O VI features as diagnostic of the accretion flow in symbiotic stars, studies of fundamental properties on the conversion efficiency are of importance for proper interpretation of spectroscopic data. A pioneering and fairly comprehensive work using a Monte Carlo technique was presented by Schmid (1992), who included angular distribution and polarization in his simulations. Basic scattering geometries such as an illuminated slab and sphere were considered to reveal the systematic changes in flux and polarization expected in a binary orbital motion. Schmid (1996) and Lee & Lee (1997a) also presented more extended studies of Raman scattered O VI in scattering geometries that include an expanding H I region around the giant component.

Despite these sophisticated and extensive previous works, we assert that useful information regarding a representative H I column density around the giant component can be gained through simple Monte Carlo simulations, which we present in this paper. We focus on the dependence on the H I column density of the flux ratio of Raman features at 6825 Å and 7082 Å in a few simple scattering geometries.

This paper is composed as follows. In Section 2 we describe the scattering geometry and the Monte Carlo procedures. We present our results in Section 3. In Section 4, we present our high resolution spectra of the two symbiotic stars AG Draconis and HM Sagittae obtained with the *Canada-France-Hawaii Telescope* to infer the characteristic H I column density in these systems. We conclude and discuss observational implications in the final section.

2. Monte Carlo Procedures

In this work, we consider three types of geometric configuration for the neutral region, which are planar, cylindrical and spherical. The neutral region is assumed to be static and of uniform H I density n_{HI}. The neutral slab considered in this work has a finite thickness H along the z-axis and is of infinite extent in the two lateral directions taken to be the $x-y$ directions. The cylinder has an infinite length along the x-axis and the circular section in the $y-z$ plane is specified by the radius R. For each geometric shape, two cases are considered for the location of a point-like and isotropic O VI emission source. In the first case we embed the O VI emission source at the center of the neutral region. The second case is that the O VI source is outside the neutral region.

Fig. 2 shows schematically the scattering geometry and the coordinate system adopted in this work. The top 3 panels correspond to the first case that the O VI source is located at the center of the neutral region. The bottom 3 panels illustrate the second case where the neutral region is illuminated by the O VI source located on the $z-$axis. In the cylinder case, the O VI source is located in such a way that the radius of the circular section cut by the $y-z$ plane subtends an angle of 20°. Similarly in the case of the illuminated sphere, the radius R subtends the same angle of 20°.

The scattering geometry is fully specified by determining the H I column density N_{HI} along a designated direction. For example, the slab geometry is specified by setting $N_{HI} = n_{HI}H$ along the slab normal which coincides with the z-axis. In the cases of the cylinder and sphere geometry, we set $N_{HI} = n_{HI}R$.

In this work, we also make a simple assumption that the neutral region is optically thin for optical photons so that once Raman scattering takes place the scattered photon leaves the region to without further interaction reach the observer. This assumption implies that in a neutral region with a very high N_{HI} the expected mean number of Rayleigh scatterings for an O VI line photon is given by the inverse of the branching ratio, which is 5.5 for O VIλ1032 and 3.7 for O VIλ1038.

Our Monte Carlo simulation starts with a generation of an O VI line photon. In this work, we assume that the O VI emission is isotropic and monochromatic at two frequencies corresponding to the line centers of O VI$\lambda\lambda$ 1032 and 1038. Two uniform random numbers r_1, r_2 in the interval $(0, 1)$ are generated to obtain an isotropic unit wavevector $\hat{\mathbf{k}}$ associated with the initial photon

$$\hat{\mathbf{k}} = (\sin\theta\cos\phi, \sin\theta\sin\phi, \cos\theta) \qquad (4)$$

with $\theta = \cos^{-1}(2r_1 - 1)$ and $\phi = 2\pi r_2$.

The physical distance s traveled by an O VI line photon is related to the optical path length τ by

$$s = \tau/(n_{HI}\sigma_{tot}), \qquad (5)$$

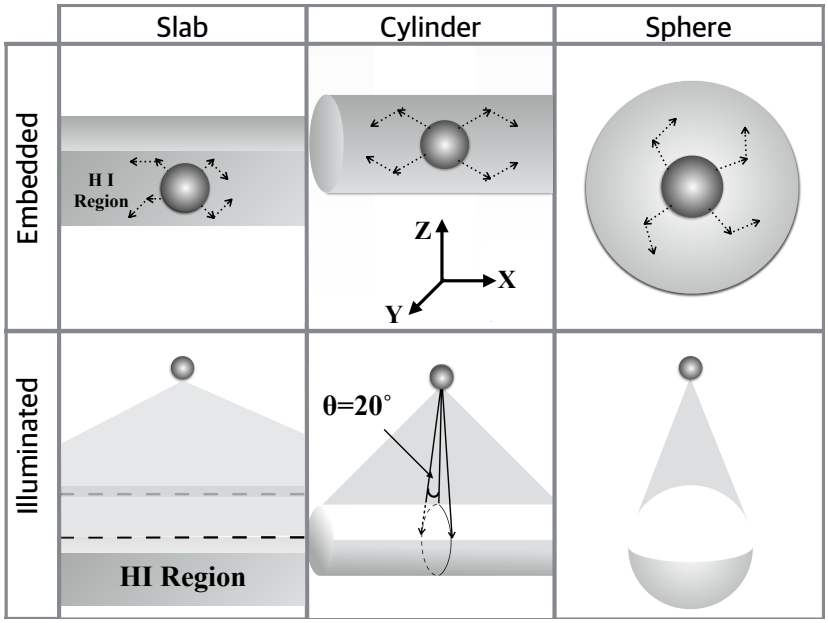

Fig. 2.— Scattering geometry and the coordinate system considered in this work. The neutral region takes a shape of a slab, a cylinder or a sphere. The top 3 panels correspond to the cases where the O VI emission source is embedded at the center of the H I region. In the bottom 3 panels, the O VI emission source is outside the neutral region. The emission source is on the z-axis. In the cylinder and sphere cases, the circular radius subtends an angle of 20° with respect to the O VI emssion source.

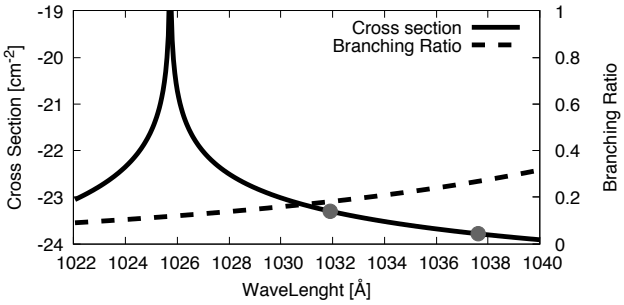

Fig. 1.— Cross section and branching ratio for Raman scattering into $2s$ in a wavelength interval 1022 Å $< \lambda <$ 1040 Å. The left vertical axis shows the logarithm of the cross section and the right vertical axis shows the branching ratio. The branching ratio is an increasing function of wavelength in this interval.

where $\sigma_{tot} = \sigma_{Ray} + \sigma_{Ram}$ is the total scattering cross section of the O VI line photon. Subsequently, the next scattering site $\mathbf{r}_f$ from the initial position $\mathbf{r}_i$ is determined by

$$\mathbf{r}_f = \mathbf{r}_i + s\hat{\mathbf{k}}. \tag{6}$$

If $\mathbf{r}_f$ is inside the scattering region, a new scattering is made. Because the same scattering phase function is shared by both Rayleigh and Raman scattering processes (e.g. Schmid & Schild 1990; Lee & Lee 1997a), we select a new unit wavevector before we determine the scattering type on the basis of the branching ratio.

A density matrix formalism is adopted to select the new unit wavevector, which is explained in the literature (e.g., Chang et al. 2015; Ahn & Lee 2015). Even though we disregard the polarization of the emergent Raman scattered radiation in this work, each photon in our Monte Carlo simulation is traced until escape and detection by an observer with polarization information retained. The density matrix associated with a photon in this simulation is a 2×2 Hermitian matrix ρ car-

rying the same information as the set of 4 Stokes parameters I, Q, U and V. One representation can be written as

$$\rho_{11} = \frac{I+Q}{2}, \quad \rho_{22} = \frac{I-Q}{2}, \quad \rho_{12} = \frac{U+iV}{2}. \tag{7}$$

Here, in this work no circular polarization is considered and $V = 0$. The basis vectors for linear polarization are chosen in the following way

$$\begin{aligned} \hat{\mathbf{e}}_1 &= (-\sin\phi, \cos\phi, 0) \\ \hat{\mathbf{e}}_2 &= (\sin\theta\cos\phi, \sin\theta\sin\phi, \cos\theta), \end{aligned} \tag{8}$$

where $\hat{\mathbf{e}}_1$ and $\hat{\mathbf{e}}_2$ indicate the polarization direction perpendicular and parallel to the $z-$axis, respectively.

The unnormalized density matrix elements associated with the scattered radiation is given by

$$\rho'(\mu, \phi, \mu'\phi')_{kl} = \sum_{i,j=1}^{2} |\hat{\mathbf{e}}'_k \cdot \hat{\mathbf{e}}_i| \rho_{ij} |\hat{\mathbf{e}}_j \cdot \hat{\mathbf{e}}'_l|. \tag{9}$$

The unnormalized probability density function describing the angular distribution of the scattered radiation is obtained by taking the trace of the density matrix associated with the scattered radiation $\rho'_{11} + \rho'_{22}$, which is explicitly given by

$$\begin{aligned} Tr(\rho') &= \rho'_{11} + \rho'_{22} \\ &= \rho_{11}(\cos^2\Delta\phi + \mu'^2 \sin^2\Delta\phi) + \rho_{12}[-\mu \sin 2\Delta\phi \\ &+ \mu'(\mu\mu' \sin 2\Delta\phi + 2\sqrt{1-\mu^2}\sqrt{1-\mu'^2}\sin\Delta\phi) \\ &+ \rho_{22}[\mu^2 \sin^2\Delta\phi + (\mu\mu'\cos\Delta\phi \\ &+ \sqrt{1-\mu^2}\sqrt{1-\mu'^2})^2] \end{aligned} \tag{10}$$

Typically we generate 10^6 line photons for each data point. In this work, we do not consider the angular distribution of Raman scattered radiation and collect all the emergent Raman photons.

3. Result

3.1. Slab

In Fig. 3, we show our Monte Carlo results for Raman scattered O VI formed in a neutral region with a slab geometry. The left 3 panels correspond to the cases where the emission source is embedded at the center of the slab, and the right 3 panels are for the case where the emission source is outside the slab. The horizontal axis is the logarithm of

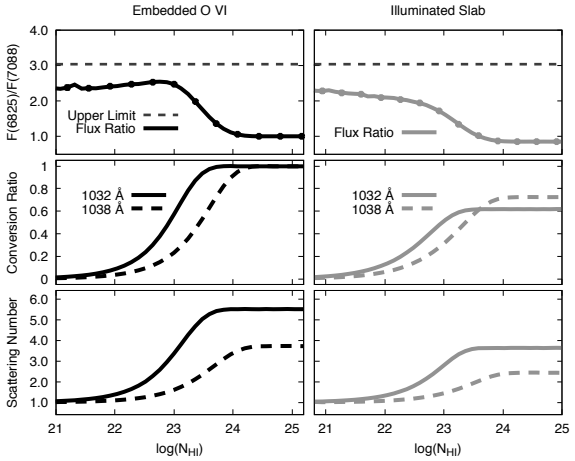

Fig. 3.— Flux ratio, Raman conversion efficiency and mean scattering number of Raman scattered O VI emergent from a slab with a finite thickness and infinite lateral dimensions. The left 3 panels and right 3 panels correspond to the cases where the O VI source is embedded at the center of the slab and outside the slab, respectively. The horizontal axis is the logarithm of H I column density measured along the slab normal. The top panels show the flux ratio of Raman 6825 and Raman 7082. The horizontal dotted line in each top panel shows the ratio $\sigma_{Ram}(1032)/\sigma_{Ram}(1038) = 3.04$. The middle panels show the Raman conversion rate, and the bottom panels show the mean number of scatterings before escape the neutral region.

$N_{HI} = n_{HI}H$, where H is the thickness of the slab.

The top panels show the flux ratio $F(6825)/F(7082)$. The values obtained through Monte Carlo calculations are shown by small circles that are connected by a solid curve. The horizontal dashed line indicates the ratio of Raman scattering cross sections for O VI$\lambda\lambda$ 1032 and 1038, which is 3.04. This is the flux ratio naively expected in a very optically thin scattering region. In the middle panels, we plot the Raman conversion efficiency, where the solid and dotted curves are for Raman O VI features at 6825 Å and 7082 Å, respectively. The bottom panels show the mean scattering number. It should be noted that the minimum number of scatterings is one for Raman scattered photons due to the inelastic nature of Raman scattering.

As N_{HI} increases, the middle panels show that more and more fractions of O VI line photons are Raman converted to escape from the slab. In the case of the embedded O VI source, the conversion efficiency approaches unity. The conversion efficiency in excess of 0.99 is reached for $N_{HI} \sim 10^{23.5}$ cm^{-2} and 10^{24} cm^{-2} for O VIλ1032 and 1038, respectively. In this optically thick limit, the mean number of scatterings before Raman conversion is given by the inverse of the branching ratio into Raman scattering. For O VIλ1032 and 1038, it is 5.5 and 3.7, respectively, which is found in the bottom left panel in Fig. 3.

In the case where the O VI emission source is outside the H I slab, as N_{HI} increases, the Raman conversion rate converges to 0.62 and 0.72 for O VIλ1032 and 1038, respectively. In this case a significant fraction $\sim 1/3$ of incident O VI photons escape from the slab via Rayleigh scattering near the surface facing the O VI source. This is also confirmed from the work of Lee & Lee (1997b), who presented their result in terms of the parameter $R_{Ram} \sim 2$ defined as the number ratio of Raman photons and Rayleigh photons emergent from a slab with the total scattering optical depth $\tau_s = 10$. This implies that roughly one third of incident O VI photons will escape through Rayleigh scattering. They considered Raman scattering processes of a hypothetical UV photon with the Raman branching ratio of 0.2, which is slightly larger than that for O VIλ1032 and smaller than that for O VIλ1038.

Rayleigh escape is more effective for O VIλ1032 than O VIλ1038, which is attributed to the larger Rayleigh branching ratio of O VIλ1032. Escape via Rayleigh scattering is significantly contributed by reflection events at first scattering site near the illuminated surface, which, in turn, is sensitive to the branching ratio. As is illustrated in the top right panel, this Rayleigh reflection effect suppresses the formation of the Raman 6825 feature more than the Raman 7082 feature in this high N_{HI} limit, which results in the flux ratio approaching a value ~ 0.85 smaller than unity. A comparison of the bottom panels shows that the mean scattering number is lower in the illumination case, because photons escaping from shallow regions of the illuminated surface are characterized by a small number of scatterings.

In the top panels, another interesting behavior in the flux ratio is noted in the optically thin limit, which is that the flux ratio is not convergent to the ratio of Raman scattering cross sections but remains significantly below it. It appears that the flux ratio converges to a value ~ 2.3 for both cases. Because of the infinite extent in the $x-y$ directions, scattering optical depth for O VI photons traveling in the grazing direction can be significant, leading to a mean number of scatterings slightly larger than 1, as shown in the bottom panels. While an O VI line photon can easily escape in the direction normal to the slab, there is a nonnegligible fraction of O VI photons that escape from the thin slab through a single Rayleigh scattering. Escape through a single Rayleigh scattering can be made more readily by O VIλ1032 photons than O VIλ1038 ones due to larger branching ratio into Rayleigh scattering of O VIλ1032. This accounts for the flux ratio of 2.3 in the small N_{HI} limit, which is smaller than the value of 3.05, the ratio of Raman scattering cross sections.

As is shown in the top right panel, the flux ratio monotonically decreases in the case where the O VI source is outside the slab. However, the flux ratio forms a broad hump peaking at ~ 2.5 near $N_{HI} = 10^{22.5}$ cm^{-2} in the case where the O VI source is embedded in a neutral slab. At this H I column density, the total scattering optical depth for O VIλ1032 is near unity, whereas O VIλ1038 remains Rayleigh-Raman optically thin. A nonlinear behavior between the mean scattering number and N_{HI} becomes significant for O VIλ1032, while a linear relation prevails for O VIλ1038.

3.2. Cylinder

Fig. 4 shows our Monte Carlo results for Raman scattered O VI formed in cylindrical neutral regions. The left 3 panels are for the case where the O VI emission source is embedded at the center of the cylinder. The flux ratio approaches the ratio of Raman scattering cross sections in the low N_{HI} limit, as is shown in the top left panel. It is noted that escape through Rayleigh scattering is almost negligible in the cylindrical neutral region. As in the case of the slab geometry with the emission source embedded, there is also a broad hump near $N_{HI} \sim 10^{22.5}$ cm^{-2} with the peak value of ~ 3.2. As N_{HI} increases, the flux ratio approaches unity, which implies the full conversion into Raman optical photons. This is confirmed by the Raman conversion efficiency convergent to unity shown in the left middle panel. The mean scattering number also converges to the inverse of Raman branching ratio considered in the slab case.

In the right 3 panels, we show our Monte Carlo result for a cylindrical neutral region illuminated by an O VI emission source. As shown in the top right panel, the flux ratio monotonically decreases from the expected optically thin limit of 3.05 to a value ~ 0.87 as N_{HI} increases. Again in this case Rayleigh reflection occurs near the boundary region facing the O VI source, which lowers the flux ratio to ~ 0.87 in the optically thick limit. This value is slightly larger than that obtained in the slab case considered in Fig. 3. The Rayleigh reflection effect is contributed by those photons incident in the grazing direction, of which the fraction is lower for a cylindrical geometry than for a slab geometry. This is also confirmed from the fact that the scattering numbers for O VIλ 1032 and 1038 in the case of an illuminated cylinder are larger than those values corresponding to the illuminated slab case.

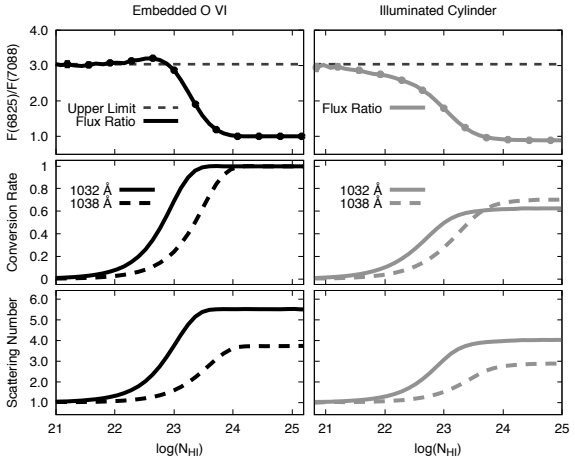

Fig. 4.— The same quantities for a cylindrical neutral region as in Fig. 3. The left 3 panels are for the results for the O VI emission source embedded at the center of the cylinder. The right 3 panels are for the case where the O VI source is outside the cylinder with the cylinder diameter subtending an angle of 20° with respect to the O VI source.

3.3. Sphere

Fig. 5 shows our Monte Carlo result for Raman scattered O VI formed in a spherical neutral region. The left 3 panels are for the case where the emission source is embedded at the center. In the optically thin limit, the flux ratio is convergent to the ratio of Raman scattering cross sections. In the opposite case of an extremely high optical depth, the flux ratio approaches unity, which in-

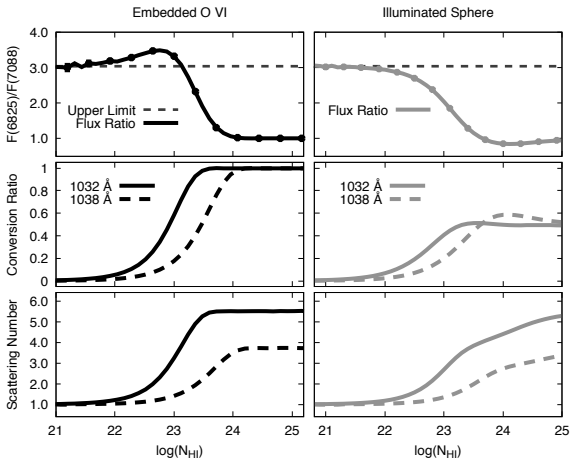

Fig. 5.— The same quantities for a spherical neutral region as in Fig. 3. The left 3 panels are for the results for the O VI emission source at the center of the sphere. The right 3 panels are for the case where the O VI source is outside the sphere with the diameter subtending an angle of 20° with respect to the O VI source.

dicates the complete Raman conversion. We also note that the mean number of scatterings also converges to the expected values, which are inverses of the branching ratios.

In this figure, a particularly notable feature is the broad bump appearing at around $N_{HI} = 10^{22.7}$ cm^{-2}. The peak value is approximately 3.5, a value significantly in excess of the ratio of Raman scattering cross sections. The value of 3.5 is also the maximum flux ratio obtained in this work. Considering the fact that the flux ratio $F(1032)/F(1038)$ of O VIλ1032 and O VIλ1038 is 2 in an optically thin O VI nebular region, the largest value of the flux ratio $F(6825)/F(7082)$ that would be observed is about 7.

The right 3 panels show the Monte Carlo result for the case where the emission source is outside the sphere, illuminating it from a distance where the diameter of the H I region subtends an angle of 20°. In the optically thin limit, the flux ratio approaches the ratio of Raman scattering cross sections. In the limit of high optical depths the Rayleigh reflection effect is working so that the flux ratio approaches 0.9, a value slightly less than unity.

It is also interesting to note the presence of a dip feature around $N_{HI} = 10^{24}$ cm^{-2} in the top right panel instead of the broad hump present in the top left panel in Fig.5. The broad hump and dip features appearing in the top left and right panels of Fig.5, respectively, are attributed to the nonlinear behavior of the Raman conversion efficiency as a function of N_{HI} near unity of the Rayleigh-Raman scattering optical depth for O VIλ1032 or O VIλ1038.

3.4. Finite Cylinder Model

In Fig. 6, we present our result where the scattering region takes the form of a cylinder with a finite height H and a radius R. The horizontal axis is the logarithm of H I column density $N_{HI} = n_{HI}H$ measured along the cylinder axis. We show the results for 4 values of $R/H = 1/5000$, 1, 5 and 5000. In the top panel, the O VI source lies at the center of the neutral region. In the bottom panel, the O VI source is located on the extension of the cylinder axis illuminating the top circle at a distance amounting to the radius R.

The cases of $R/H = 1/5000$ and 5000 are effec-

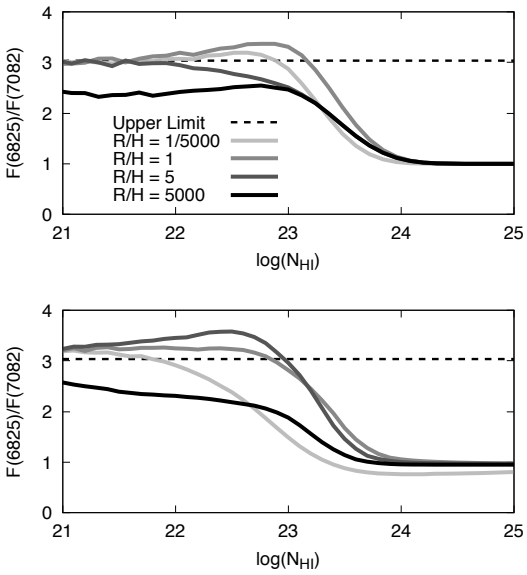

Fig. 6.— Flux ratio $F(6825)/F(7082)$ of Raman scattered O VI emergent from a cylindrical neutral region. The cylinder has a radius R and a height H. Four values of $R/H = 1/5, 000, 1, 5$ and 5,000 are considered. The emission source is located at the center of the cylinder in the top panel. In the bottom panel, the O VI source is located on the extension of the cylinder axis illuminating the top circle at a distance where the diameter subtends a right angle. The horizontal axis is the logarithm of N_{HI} along the cylinder axis so that $N_{HI} = n_{HI}H$.

tively the same as those of the cylinder and slab models, respectively, which we considered in the previous subsections. The case of $R/H = 1$ also mimics the sphere model, in which the maximum flux ratio of 3.5 is obtained. In these three cases a broad bump appears near $N_{HI} = 10^{22.5}$ cm^{-2}. However, as is shown in the case of $R/H = 5$, the flux ratio monotonically decreases from the optically thin limit of 3 to the optically thick limit of 1.

As R/H increases from a very small value of $\sim 1/5000$ to a moderate value ~ 1, the change in flux ratio occurs mainly in the transitional regime around $N_{HI} \sim 10^{23}$ cm^{-2}, where the flux ratio $F(6825)/F(7082)$ shows an overall increase. As R/H further increases from 1 to 5, a significant decrease in the flux ratio is made near $N_{HI} = 10^{23}$ cm^{-2}, which results in an overall monotonic decrease of $F(6825)/F(7082)$ in the entire range of N_{HI}. Now as R/H increases sufficiently, Rayleigh escape lowers the flux ratio in the regime $N_{HI} < 10^{23}$ cm^{-2} resulting in the overall flux ratio ~ 2.3 obtained in the slab case in the optically thin limit.

In the bottom panel there are a few interesting points to be noted. The first point is that when $R/H = 5$ there appears a broad bump at $N_{HI} = 10^{22.6}$ cm^{-2} with a peak value ~ 3.5. Considering a similar high value is obtained in the sphere case with an embedded O VI source, caution should be exercised to interpret observed flux ratios of Raman O VI features. Another point is that when $R/H = 1$ the behavior is similar to that found for a neutral sphere illuminated outside considered in Fig. 5. Finally as is found in the illuminated slab case, the effect of Rayleigh escape is clearly seen in the case $R/H = 1/5,000$, where $F(6825)/F(7082)$ remains ~ 0.8 for $N_{HI} \geq 10^{24}$ cm^{-2}.

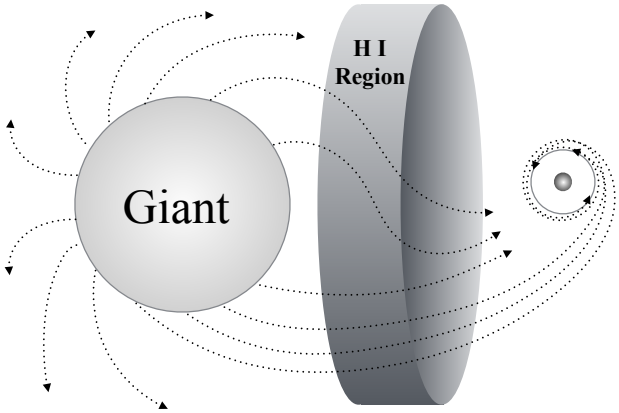

Fig. 7.— A schematic illustration of Raman scattering geometry adopted in this work for a symbiotic star. We adopt a highly simplified neutral region delineated by a finite cylinder with $R/H = 5$ in front of the giant component. The diameter of the neutral cylinder is set to equal the binary separation. The circular boundary of the H I region facing the white dwarf cuts the binary axis at its midpoint so that the diameter subtends an angle of 90° with respect to the white dwarf.

4. Comparison of Simulated and Observed Spectra

4.1. Simulated Spectra

In this subsection, we produce mock spectra of Raman scattered O VI using a toy model of a symbiotic star. A schematic illustration of the Raman scattering geometry is shown in Fig. 7. A fraction of the slow stellar wind from the giant component is accreted through gravitational capture by the white dwarf. We place the neutral region in front of a giant and set up an O VI emission line region

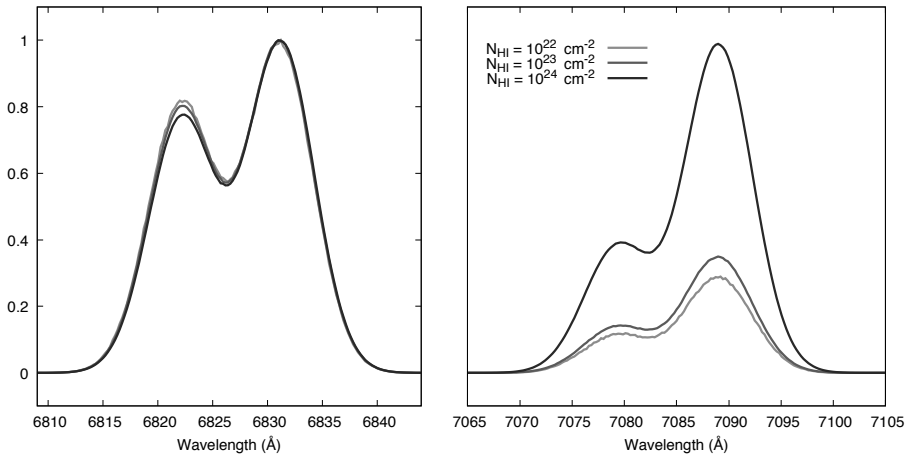

Fig. 8.— Mock spectra of Raman scattered O VI$\lambda\lambda$ 1032 and 1038 formed in in the scattering geometry shown in Fig. 7. The left panel is Raman O VI feature at 6825 Å and the right panel is for Raman O VI at 7082 Å.

around the white dwarf component.

A realistic neutral region is expected to take a shape that may be approximated by a hyperboloid (e.g. Taylor & Seaquist 1984; Lee & Kang 2007). However, in this work we adopt a much simpler geometry of a finite cylinder in order to focus on the issue of the flux ratio. In particular, we fix the ratio $R/H = 5$ of the cylinder radius R and height H. We set the diameter of the cylindrical neutral region equal to the binary separation. In fact, this geometry was considered in Fig. 6.

Lee & Park (1999) proposed that multiple peak structures and disparity of Raman O VI features can be understood if the O VI emission region is a part of the accretion flow around the white dwarf component. The accretion flow is expected to be convergent on the entering side, from which the red part of the Raman O VI feature is formed. On the opposite side, the flow tends to be divergent partially colliding with the slow stellar wind from the giant. In the optically thin region, O VIλ1032 is expected to be twice stronger than O VIλ1038 due to twice larger statistical weight for $s_{1/2}-p_{3/2}$ transition than $s_{1/2}-p_{1/2}$. However, thermalization dictates that O VI$\lambda\lambda$1032 and 1038 tend to be of similar strength in the optically thick limit (e.g., Schmid et al. 1999). Combining this fact with the asymmetric accretion flow with the entering side much thicker than the opposite side, we expect that the blue part of Raman 7082 should be more suppressed compared to its red part than that of Raman 6825.

Lee & Kang (2007) performed profile analyses of Raman O VI 6825 fluxes for two 'D' type symbiotic stars, V1016 Cygni and HM Sagittae. They successfully showed that the profiles are consistent with the Keplerian motion of the O VI emission region around the white dwarf component with a typical speed of ~ 30 km s^{-1}. A similar result is also obtained by Heo & Lee (2015), who investigated the disparity in the profiles of Raman O VI features. We assume that the O VI emission region is asymmetric in such a way that the entering side of the stellar wind is significantly denser than the opposite side. For the sake of simplicity, it is assumed that the O VI emission region is perfectly divided into the two regions, that are the red and blue emission regions.

Furthermore, we assume that the O VI line profile viewed from the neutral region is an asymmetric double Gaussian function, where each Gaussian component describes either the blue or the red emission region. According to Lee & Kang (2007), the velocity difference of the two peaks in the Raman O VIλ 6825 feature of the symbiotic star V1016 Cyg is about 60 km s^{-1}. This separation corresponds to the observed width of ~ 10 Å which is typical for most symbiotic stars exhibiting Raman O VI features. In this work, we set the full width at half maximum of the Gaussian profile

function to be $\Delta v = 20$ km s^{-1}. In addition, we prepare the incident O VIλ1032 with the blue peak flux 80 percent weaker than the red peak. As Heo & Lee (2015) proposed, we simply assume that the red emission region is characterized by the flux ratio $F(1032)/F(1038) = 1$ of O VI$\lambda\lambda$ 1032 and 1038 resonance doublet whereas $F(1032)/F(1038) = 2$ in the blue emission region. Therefore, the ratio of the blue and red peaks for O VIλ1038 is 0.4.

In Fig. 8 we show the mock spectra obtained from our Monte Carlo simulations based on the simple model illustrated in Fig. 7. Here, we obtain Raman O VI photons for various values of N_{HI} of the neutral region in the shape of a finite cylinder. The H I column density is measured along the cylinder axis so that $N_{HI} = n_{HI}H$. In this figure, we present the results for 3 different values of $\log N_{HI} = 22, 23$ and 24. The left and right panels show the profiles of Raman O VI features at 6825 Å and 7082 Å, respectively. The vertical axis is a relative flux density and we normalize the profile so that the maximum of Raman O VI at 6825 has the unit value.

In the left panel, it is noted that the profiles of Raman 6825 O VI feature differ for different values of N_{HI}. As N_{HI} increases, the blue component tends to be increasingly suppressed relative to the red component. This slight variation is attributed to the decrease of scattering cross section near 1032 Å as the wavelength increases. The blue and red peaks occur at $\lambda = 1031.809$ Å and 1032.015 Å, respectively, where the relative decrease in cross section is about 6 percent and the relative increase in branching ratio is only 0.1 percent. This implies that the decrease in the cross section is mainly responsible for the variation of the blue peak relative to the red peak amounting to 4 percent.

In the right panel, we note a significant flux variation in Raman O VI 7082. In the high column density limit, the red peaks of Raman 6825 and Raman 7082 are comparable. In the opposite limit of low column density the flux ratio of the red peaks approaches 3.47, the ratio of Raman scattering cross sections.

4.2. *CFHT* Spectra

In Fig. 9, we show our spectra around Raman O VI features of two symbiotic stars HM Sge (top panels) and AG Dra (bottom panels) obtained with ESPaDOnS installed on the 3.6 m *Canada-France-Hawaii Telescope*. The observation of HM Sge and AG Dra was made on 2014 August 16 and September 6, respectively . HM Sge was observed in spectropolarimetric mode for which the spectral resolution is 68,000. In the case of AG Dra, we choose 'object only' spectroscopic mode for which the spectral resolution is 81,000. The total integration time for HM Sge and AG Dra was 9,600 s and 2,000 s, respectively. HM Sge is a 'D' type symbiotic star, having a Mira variable as giant companion, whereas AG Dra is an 'S' type symbiotic star with an orbital period of 550 days (e.g. Fekel et al. 2000).

HM Sge is known to have erupted as a symbiotic nova in 1975 (Dokuchaeva 1976). It is also known to exhibit Raman scattered features of O VI and He II (e.g. Birriel 2004; Lee & Kang 2007). Based on their spectropolarimetric monitoring observations, Schmid & Schild (2002) proposed that the orbital period of HM Sge amounts to ~ 50 years with a caveat that the data quality was insufficient for definite conclusion. AG Dra is known to be a yellow symbiotic star having an early K type giant as mass donor (e.g. Leedj ä rv et al. 2016)

In the top panels for HM Sge, the simulated profiles are obtained adopting the same finite cylinder model with $N_{HI} = 10^{22}$ cm^{-2} considered in the previous subsection. On the other hand, in the bottom panels, a finite cylinder model with $N_{HI} = 10^{23.3}$ cm^{-2} is used with the other conditions the same as in the top panels. We obtain relatively poor fit of the Monte Carlo simulated profiles to the *CFHT* spectra. However, the purpose of the current profile comparison is not a detailed profile fit but a simple estimate of the representative neutral column density of the scattering region from the ratio $F(6825)/F(7082)$. From this comparison, it is clear that AG Dra is characterized by a neutral region with N_{HI} an order of magnitude larger than that of HM Sge. We suggest that this is attributed to the closeness of the giant component to the white dwarf in 'S' type symbiotic stars.

As Schmid et al. (1999) explained in their observations of a number of symbiotic stars, 'S' type symbiotics systematically show higher Raman conversion efficiency than 'D' type symbiotics. Based on near simultaneous far UV and optical

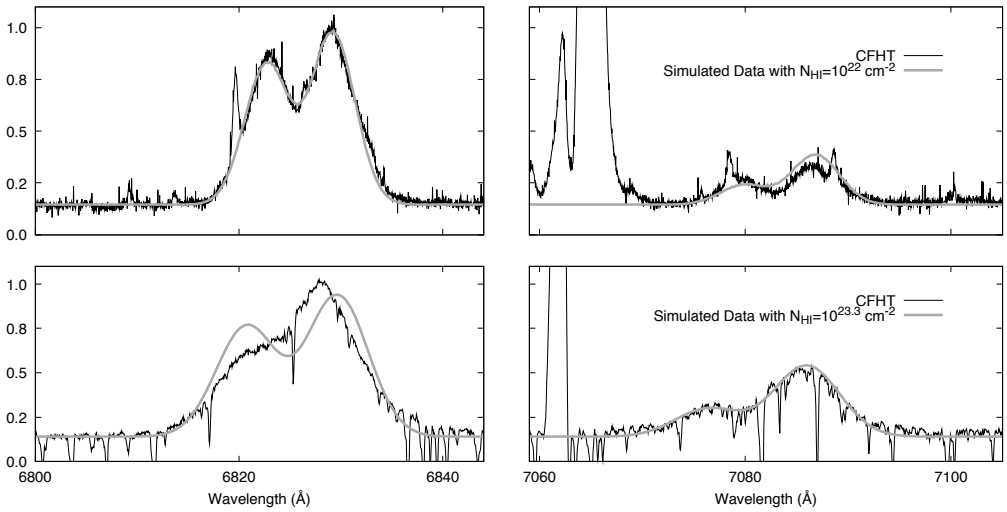

Fig. 9.— *CFHT* spectra of Raman scattered O VI$\lambda\lambda$ 1032 and 1038 near 6825 Å and 7082 Å of a 'D' type symbiotic star HM Sge (top panels) and an 'S' type symbiotic star AG Dra (bottom panels). Profiles obtained from our Monte Carlo simulations are overplotted to the *CFHT* data.

spectroscopic observations, Birriel et al. (2000) also summarized in their Table 11 higher ratios $[N_{6825}/N_{1032}]/[N_{7082}/N_{1038}]$ in 'S' type symbiotics such as Z And and AG Dra than in 'D' type symbiotic stars V1016 Cyg and RR Tel.

5. Discussion

5.1. Flux Ratio $F(6825)/F(7082)$

In this work, we have investigated the flux ratio $F(6825)/F(7082)$ using a Monte Carlo technique mainly as a function of N_{HI} for a few simple scattering geometries. The smallest flux ratio of $F(6825)/F(7082) \sim 0.8$ is obtained when the emission source is outside a neutral slab with infinite lateral dimensions and Rayleigh-Raman optically thick in the normal direction. In this case, a significant fraction of O VI photons escape from the neutral region through a few Rayleigh scatterings near the illuminated boundary. On the other hand, the maximum flux ratio of 3.5 is obtained in the case of a spherical neutral region with a moderate column density of $N_{HI} \sim 10^{22.7}$ cm^{-2} inside which the O VI emission source is embedded. This maximum value is attributed to a nonlinear behavior shown in Raman conversion of O VIλ1032 whereas O VIλ1038 remains in the linear domain.

According to Espey et al. (1995) the flux ratios of $F(1032)/F(6825) \simeq 12$ and $F(1038)/F(7082) \simeq 36$ measured for the symbiotic star RR Tel correspond to our result $F(6825)/F(7082) \simeq 3$ in this work in which we fix the number flux $F(1032)/F(1038) = 1$. The ratio of Raman conversion efficiencies $\simeq 3$ strongly implies that the neutral scattering region is characterized by $N_{HI} < 10^{23}$ cm^{-2}. Another notable point is that the flux ratio in the optically thin limit may be irrelevant to real observations because Raman fluxes are very weak. If we require Raman conversion efficiency of > 0.1, then the representative column density of the neutral region around RR Tel is suggested to be found in the range $N_{HI} = 10^{22-23}$ cm^{-2}.

Attenuation of far UV radiation due to Rayleigh scattering in symbiotic stars is useful in estimating the neutral column density of the giant atmosphere (e.g. Isliker et al. 1989; Schmutz et al. 1994; Shagatova et al. 2016). Along a line of sight from the white dwarf to the giant photosphere, it is expected that $N_{HI} > 10^{24}$ cm^{-2}. For example, Shagatova et al. (2016) proposed a neutral column density $N_{HI} \sim 10^{25}$ cm^{-2} toward the giant atmosphere of the symbiotic star EG And based on their measurement using *IUE* and *HST* spectra. From this work, we propose that the flux ratio $F(6825)/F(7082)$ can be a rough proxy to

estimate N_{HI} in symbiotic stars.

5.2. H I Column Density

With the giant companion being closer to the white dwarf primary, 'S' type symbiotics tend to be in a more favorable condition to establish a neutral scattering region with significantly higher N_{HI} than 'D' type symbiotics. This leads to the ratio $F(6825)/F(7082)$ systematically larger in 'D' type symbiotics than in 'S' type symbiotics, which was pointed out by Schmid et al. (1999). However, not only the separation between the binary components, but also very different properties of the wind from cool components in S-type and D-type symbiotics can affect their H I region.

A crude estimate of the representative N_{HI} can be given by assuming that the mass loss process is characterized by a spherical stellar wind with velocity field at a radial distance r from the giant

$$v(r) = v_\infty \left(1 - \frac{R_*}{r}\right)^\beta. \quad (11)$$

Here, v_∞ is the wind terminal velocity, β is a parameter of order unity and R_* is the launching radius of the giant stellar wind (e.g. Lamers & Cassinelli 1999). A line of sight from the white dwarf is specified by the impact parameter b with respect to the giant. If we disregard the photoionization process due to strong far UV radiation from the white dwarf, the H I column density along this line is given by

$$N_{HI} = \frac{2\dot{M}}{4\pi\mu m_p v_\infty} \int_b^\infty \frac{dr}{(r - R_*)\sqrt{r^2 - b^2}}, \quad (12)$$

with the choice of $\beta = 1$ and $b > R_*$ (Nussbaumer & Vogel 1989). Here, μ is the mean molecular weight of the giant stellar wind. Whereas the definite integral is explicitly written as

$$N_{HI} = \frac{\dot{M}}{\pi\mu m_p v_\infty \sqrt{b^2 - R_*^2}} \left[\frac{\pi}{2} - \tan^{-1}\sqrt{\frac{b - R_*}{b + R_*}}\right], \quad (13)$$

a more useful approach is to obtain a rough approximation by taking μ and the value in the parenthesis to be unity (e.g. Lee & Kang 2007). We may take a typical impact parameter b as the binary separation A. In the case of 'D' type symbiotics $A \gg R_*$, whereas for 'S' type symbiotics the binary separation b is comparable to or a few times R_*. With this consideration we may write

$$N_{HI} \sim \left(\frac{\dot{M}_7}{v_{10} A_{14}}\right) 10^{22} \text{ cm}^{-2} \quad (14)$$

where $\dot{M}_7 = 10^{-7} M_\odot$ yr^{-1}, $v_{10} = v_\infty/[10$ km s$^{-1}]$ and $A_{14} = A/10^{14}$ cm.

Seaquist & Taylor (1990) proposed that the mass loss rate is correlated with the spectral type in such a way that later spectral type giants tend to lose mass faster (see also Seaquist et al. 1993). In the case 'D' type symbiotic star HM Sge, our result of $N_{HI} \sim 10^{22}$ cm^{-2} implies a relation $\dot{M}_7/(v_{10}A_{14}) \sim 1$. Considering that the orbital parameters are only poorly known for most 'D' type symbiotic stars, Raman O VI spectroscopy can be of significant use in putting constraints on the orbital parameters.

5.3. Mass Loss Rate

Sekeráš & Skopal (2015) used Raman scattered He II feature at 6545 Å to give an estimate of the mass loss rate of the 'D' type symbiotic star V1016 Cygni. They proposed a mass loss rate $\sim 10^{-6}$ M$_\odot$ yr^{-1} based on their analysis. A lower estimate of 3.6×10^{-7} M$_\odot$ yr^{-1} was proposed by Jung & Lee (2004), who used the center shift of Raman scattered He II feature at 4850 Å attributed to the atomic physics of Raman scattering. Their estimate was $N_{HI} = 4 \times 10^{21}$ cm^{-2}, which is quite small for effective Raman conversion of O VI. Because the line center of Raman scattered He II feature can also be affected from the kinematics of the H I region with respect to the He II emission region, there is possibility that their estimate would be modified to a higher H I column density.

Considering that He II$\lambda\lambda$1025 and 972 have cross sections $\sim 10^{-22}$ cm^2, we may expect higher Raman conversion efficiencies in the formation of Raman He II features at 6545 Å and 4850 Å than O VI lines. For He IIλ949, the cross section $\sim 10^{-21}$ cm^2 is significantly smaller than the two lower transition lines, leading to lower Raman conversion efficiency. One complicating factor in the analysis of Raman scattering involving He II is that there are many scattering branches into the IR region. Sophisticated simulations designed to

explain various Raman scattered features including O VI and He II will provide very strong constraints on the scattering geometry and mass loss rate involving the giant component.

5.4. Spectropolarimetric Implications

The difference in scattering numbers affects the degree of linear polarization as well as the flux ratio $F(6825)/F(7082)$. As the scattering number increases, the radiation field tends to be isotropized resulting in weak polarization. Schmid & Schild (1990) reported that the Raman O VI 7082 in the symbiotic star He2-38 exhibits the degree of linear polarization of 9.2 percent, which is in contrast with the much more weakly polarized Raman O VI 6825 with the degree of 5.3 percent. They pointed out that the this difference can be understood because Raman O VI 7082 photons are formed with less number of scatterings than Raman O VI 6825 photons. As is shown in this work, the mean scattering number is a complicated function of the scattering optical depth and the branching ratio.

This work will be extended to obtain Raman fluxes according to the emergent wave vector for further polarimetric analysis. It is expected that combination of these differences in flux and polarization apparent in spectropolarimetric data will be used to put strong constraints on the mass loss and transfer processes occurring in symbiotic stars.

Acknowledgements

The authors are very grateful to the anonymous referee for constructive comments. This work was supported by K-GMT Science Program (PID: 14BK002) funded through Korea GMT Project operated by Korea Astronomy and Space Science Institute. This research was also supported by the Korea Astronomy and Space Science Institute under the R&D program(Project No. 2015-1-320-18) supervised by the Ministry of Science, ICT and Future Planning.

REFERENCES

Ahn, S. -H., Lee, H.-W., 2015, Journal of the Korean Astronomical Society, 48, 195

Allen, D. A., 1980, MNRAS, 190, 75

Angeloni, R., Contini, M., Ciroi, S., Rafanelli, P., 2010, MNRAS, 402, 2075

Angeloni, R., Di Mille, F., Bland-Hawthorn, J., Osip, D. J., 2011, ApJL, 743, L8

Angeloni, R., Di Mille, F., Ferreira Lopes, C. E., Masetti, N., 2012, ApJL, 756, L21

Birriel, J. J., 2004, ApJ, 612, 1136

Birriel, J. J., Espey, B. R., Schulte-Ladbeck, R. E., 2000, ApJ, 545, 1020

Chang, S.-J., Heo, J.-E., Di Mille, F., Angeloni, R., Palma, T., Lee, H.-W., 2015, ApJ, 814, 98

Dokuchaeva, O. D., 1976, IBVS, 1189, 1

Espey, B. R., Schulte-Ladbeck, R. E, Kriss, G. A., Hamann, F., Schmid, H. M., Johnson, J. J., 1995, ApJL, 454, L61

Fekel, F. C., Hinkle, K. H., Joyce, R. R., Skrutskie, M. F., 2000, AJ, 120, 3255

Harries, T. J., & Howarth, I. D., 1996, A&AS, 119, 61

Heo, J. -E., Lee, H.-W., 2015, Journal of the Korean Astronomical Society, 48, 105

Isliker, H., Nussbaumer, H., Vogel, M., 1989, A&A, 219, 271

Jung, Y.-C., & Lee, H.-W., 2004, MNRAS, 355, 221

Lamers, H. J. G. L. M., & Cassinelli, J. P., 1999, Introduction to Stellar Winds (Cambridge: Cambridge Univ. Press)

Lee, H.-W., Kang, S, 2007, ApJ, 669, 1156

Lee, H.-W., Lee, K. W., 1997, MNRAS, 287, 211

Lee, K. W., Lee, H. -W., 1997, MNRAS, 292, 573

Lee, H.-W., & Park, M.-G., 1999, ApJL, 515, L89

Leedjärv, L., Gális, R., Hric, L., Merc, J., Burmeister, M, 2016, MNRAS, 456, 2558

Mikołajewska, M., 2012, Baltic Astronomy, 21, 5

Moore, C. E. 1979, NSRDS-NBS 3, sec8

Nussbaumer, H., Schmid, H. M., Vogel, M., 1989, A&A, 211, L27

Nussbaumer, Vogel, M., 1987, A&A, 182, 51

Saslow, W. M., Mills, D. L., 1969, PhRv, 187, 1025

Schmid, H. M., 1989, A&A, 211, L31

Schmid, H. M., 1992, A&A, 254, 224

Schmid, H. M., 1996, MNRAS, 282, 511

Schmid, H. M., Schild, H. 1990, A&A, 236, L13

Schmid, H. M., et al., 1999, A&A, 348, 950

Schmid, H. M., & Schild, H., 2002, A&A, 395, 117

Schmutz, W., Schild, H., Mürset, U. Schmid, H. M., 1994, A&A, 288, 819

Seaquist, E. R., Taylor, A. R., 1990, ApJ, 349, 313

Seaquist, E. R., Krogulec, M., Taylor, A. R., 1993, ApJ, 410, 260

Sekeráš, M., & Skopal, A., 2015, ApJ, 812, 162

Shagatova, N., Skopal, A., Cariková, Z., 2016, A&A, 588, A83

Sokoloski, J. L., Bildsten, L., 2010, ApJ, 723, 1188

Sokoloski, J. L., Bildsten, L., Ho, W. C. G. 2001, MNRAS, 326, 553

Taylor, A. R., & Seaquist, E. R. 1984, ApJ, 286, 263

Warner, B.. 1995, Catalcysmic Variable Stars, Cambridge Univ. Press, Cambridge

Whitelock, P. A., 1987, PASP, 99, 573

Zamanov, R., Latev, G., Boeva, S., Sokoloski, J. L., Stoyanov, K., Bachev, R., Spassov, B., Nikolov, G., Golev, V., Ibryamov, S., 2015, MNRAS, 450, 3958

This 2-column preprint was prepared with the AAS LaTeX macros v5.2.